CAMBRIDGE
UNIVERSITY PRESS

Research Article

The Curated ATCA Census of High-Mass Clumps (CACHMC) Legacy Survey

David Allingham[1] , James Michael Jackson[1,2,3], Taylor Hogge[4], John Scott Whitaker[4], Philippa Patterson[1], Nicholas Killerby-Smith[1,5], Jacob Askew[1,6,7] and Thomas Vandenberg[1]

[1]The University of Newcastle, Callaghan, NSW, Australia, [2]USRA/SOFIA Science Center, NASA Ames Research Center MS 252-176, Moffett Field, CA, USA, [3]Green Bank Observatory, Green Bank, WV, USA, [4]Boston University, Boston, MA, USA, [5]Australian National University, Canberra, ACT, Australia, [6]Centre for Astrophysics and Supercomputing, Swinburne University of Technology, Hawthorn, VIC, Australia and [7]Australian Research Council Centre of Excellence for Gravitational Wave Discovery (OzGrav), Hawthorn, VIC, Australia

Abstract

In order to study the structure and temperature distribution within high-mass star-forming clumps, we employed the Australia Telescope Compact Array to image the NH_3 (J,K) = (1,1) through (6,6) and the (2,1) inversion transitions, the H_2O 6_{16}-5_{23} maser line at 22.23508 GHz, several CH_3OH lines and hydrogen and helium recombination lines. In addition, 22- and 24-GHz radio continuum emission was also imaged.

The NH_3 lines probe the optical depth and gas temperature of compact structures within the clumps. The H_2O maser pinpoints the location of shocked gas associated with star formation. The recombination lines and the continuum emission trace the ionised gas associated with hot OB stars. The paper describes the data and presents sample images and spectra towards select clumps. The technique for estimating gas temperature from NH_3 line ratios is described. The data show widespread hyperfine intensity anomalies in the NH_3 (1,1) images, an indicator of non-LTE NH_3 excitation. We also identify several new NH_3 (3,3) masers associated with shocked gas. Towards AGAL328.809+00.632, the H_2O 6_{16}-5_{23} line, normally seen as a maser, is instead seen as a thermally excited absorption feature against a strong background continuum. The data products are described in detail.

Keywords: Galactic astronomy; ISM; ammonia; methanol; high-mass star formation; molecular clouds

(Received 29 September 2023; revised 25 May 2024; accepted 31 May 2024)

1. Introduction

The conversion of turbulent structures within molecular clouds into high-mass stars and star clusters, the relationship between Galactic and extragalactic star formation, and the effects of Galactic environment on star formation are fundamentally important, yet unsolved, problems in astrophysics. The two major theories for high-mass star formation are 'competitive accretion' and 'turbulent core accretion' (for review see Motte, Bontemps, & Louvet 2018); 'hierarchical collapse' is also postulated (Vázquez-Semadeni et al. 2019). These theories make distinct predictions about the initial conditions within star-forming clumps, and how the gas on approximately 1-pc 'clump' scales affects the accretion history onto the 0.05-pc 'core' scales at which individual stars form.

A number of continuum (ATLASGAL: Schuller et al. 2009; Contreras et al. 2013; BGPS: Glenn et al. 2009; Dunham et al. 2011; Aguirre 2011; CORNISH: Hoare et al. 2012; Hi-GAL: Molinari et al. 2010) and molecular line (MALT90: Jackson et al. 2013; Rathborne et al. 2016; HOPS: Walsh et al. 2011; Purcell et al. 2012) surveys identified thousands of dense molecular clumps

and characterised their physical and chemical conditions on parsec scales (e.g. Urquhart et al. 2011, 2014; Wienen et al. 2012, 2018; Guzmán et al. 2015; Billington et al. 2019). After decades of effort, these surveys have finally located the sites of current and future high-mass star formation throughout the Milky Way. Now that parsec-scale clump conditions have been measured, the next step is to examine the smaller size scales down to the 0.05 pc core scales. Observations on these smaller scales can be used to characterise the turbulent structure within the clumps and to measure the locations, temperatures, masses, and kinematics of smaller structures, down to the 0.05 pc size scales of star-forming cores.

These scales can be reached by interferometers, and much work is underway to determine the number of cores in individual clumps and their properties, especially with ALMA (e.g. ASHES: Sanhueza et al. 2019; ALMA-IMF: Motte et al. 2022; ALMAGAL: O'Neill et al. 2021). Mm-wave continuum interferometry probes the dust emission and provides measurements of dust masses and dust temperatures. Continuum observations, however, have several limitations. First, they cannot separate overlapping clouds along the line of sight. Second, they do not provide kinematic information which is necessary to trace turbulence and the accretion flows. Finally, although they probe the dust temperature, they do not probe the gas temperature, which may well be quite different in star-forming regions. Spectral line observations overcome these limitations.

The cm-wave inversion transitions of ammonia are particularly useful probes of high-mass star-forming clumps. These inversion lines all occur at roughly the same frequency ($\sim$24 GHz), yet span a large range of energy levels. With current broadband correlators, they can be observed simultaneously with the same telescope, thereby removing the need to compare data from different telescopes with different beam sizes and calibration uncertainties. The large spread of energies above ground of the various transitions also makes the line intensities sensitive to temperatures. Ammonia is thus considered an excellent 'thermometer' for dense star-forming gas. Finally, nuclear quadrupole splitting produces hyperfine lines, whose intensity ratios change as the gas becomes optically thick. Thus, ammonia inversion lines can be used to estimate column density.

The Curated ATCA Census of High-Mass Clumps Legacy Survey, hereafter CACHMC, described in this paper employs the ammonia inversion lines to measure gas temperatures, optical depths and velocities within high-mass star-forming clumps on 0.1- to 1-pc size scales for 60 clumps in various stages of evolution. CACHMC builds on previous surveys. Fifty high-mass clumps from the southern sky, originally identified in the ATLASGAL 870-μm dust continuum survey, and subsequently observed in the MALT90 survey were selected (Jackson et al. 2013; Rathborne et al. 2016), as discussed in Section 2.

CACHMC originally proposed to observe the $\sim$120 highest mass clumps ($M > 500$ M$_\odot$) in the fourth quadrant identified by ATLASGAL. Due to constraints of allotted observing time and source availability, however, not all of these sources could be efficiently observed with good image fidelity. The source selection criteria was subsequently relaxed to include a representative sample of clumps with $M > 200$ M$_\odot$. Each of these clumps is likely to form at least one high-mass star with $M > 8$ M$_\odot$ (e.g. Jackson et al. 2013). Moreover, clumps were also selected to span a range of evolutionary states. In particular, since more evolved clumps tend to be more luminous, they are typically observed far more often than clumps in earlier evolutionary phases. Clumps in early stages, therefore, tend to be under-represented in many surveys. To overcome this bias towards more evolved clumps, the CACHMC source list includes a number of colder clumps in earlier stages of evolution. The goal of the CACHMC source selection was to produce a large, representative sample of high-mass star-forming clumps that span a range of evolutionary states.

In addition to the primary probe of ammonia inversion lines, CACHMC includes additional probes of star-forming regions. For example, CACHMC observed the 22.235 GHz water maser line to indicate outflows and shocks from star-forming regions. In addition, several hydrogen recombination lines were also included to probe the ionised gas from embedded H II regions, if present. CACHMC also observed radio continuum emission that probes the free-free emission from ionised gas.

As an ATNF Legacy Project, CACHMC was undertaken to provide a large, homogeneous data set for the star formation community that will foster future archival projects. This paper primarily describes the survey and the data processing. In addition, it provides a few examples of preliminary scientific results. This paper is by no means intended as a comprehensive or exhaustive analysis of all CACHMC data products.

Details of the observation parameters and activities are given in Section 3 and the data reduction pipeline and post-processing in Sections 4 and 5, respectively. 115 masers were observed during the survey, mainly in the usual H$_2$O maser line, but also in

the ammonia (3,3) line, as well as in various methanol transitions. Details of these are given in Section 6.

Data for an example star-forming clump is provided in Section 7.1, showing the available data for AGAL337.916-00.477, a clump associated with the Nessie Nebula (Jackson et al. 2010). Some of these data were used in the analysis of Jackson et al. (2024). The paper concludes with details of the released data, available via the CSIRO's Data Access Portal, in Section 8. The released data comprises the calibrated and gridded data cubes, along with a variety of summary data (for example, RMS noise and moment maps) and derived physical properties (for example, optical depth and temperatures), as well as mid-infrared Spitzer images for context.

2. Science targets

The CACHMC survey targeted 50 high-mass molecular clumps in the southern Galactic Plane ($270^\circ < \ell < 20^\circ$, $-1^\circ < b < 1^\circ$), selected from sources originally identified by the ATLASGAL survey, and subsequently mapped and characterised by the MALT90 and HiGAL surveys (Jackson et al. 2013; Rathborne et al. 2016; Guzmán et al. 2015). Five additional high-mass clumps in very early evolutionary stages were added during the survey: AGAL302.486-00.031, AGAL313.576+00.324, AGAL316.752-00.012, AGAL317.429-00.561, and AGAL341.702+00.051. These 70-μm dark sources (indicating cold clumps with high optical depth) from the HiGAL database have been observed with ALMA as part of the ASHES project (Sanhueza et al. 2019; Li et al. 2022; Sabatini et al. 2022), and the CACHMC ammonia observations provided supplementary rotational excitation temperature information. An additional four high-mass molecular clumps in later evolutionary stages, as indicated by ammonia (3,3) maser emission, were also added: G23.33-0.30, NGC6334-I, -IV, and -V, each hosting ammonia (3,3) and water masers (Walsh et al. 2011; Kraemer & Jackson, 1995). These additional targets were observed in only two array configurations (750C and 1500C) except the NGC6334 sources (750C only) and G23.33-0.30 (all configurations). Finally, IC 443 was included as a candidate ammonia (3,3) maser site (McEwen et al. 2016); it was observed in the 750C array configuration only, but no (3,3) maser emission was detected.

The mid-IR images from the GLIMPSE (Benjamin, Churchwell, & Babler 2003; Churchwell et al. 2009) and MIPSGAL (Carey et al. 2009) surveys can be used to characterise the clump's evolutionary stage (Jackson et al. 2013). Of the 60 targets included here, 25 are classified as 'quiescent' and 27 as 'protostellar' clumps. These young clumps are promising locations at which to observe nascent massive star formation in its earliest phases. Of the remaining sources, 6 are HII regions and one (AGAL316.752-00.012) is a PDR; the evolutionary stage of IC 443 is unknown. Details of the observed sources are given in Table 1.

3. Observations

To carry out the survey, observations were made using the Australia Telescope Compact Array[a] (ATCA) in the southern winter semesters (April to September) from 2017 to 2020. A total of 84

---

[a]The ATCA is part of the Australia Telescope which is funded by the Commonwealth of Australia for operation as a National Facility managed by CSIRO.

Table 1. List of observed sources and targeted coordinates. Distances, where available, are taken from Whitaker et al. (2018) except that for G189.1+3.0 (also known as IC 443), taken from McEwen et al. (2016).

Name	Galactic longitude (deg)	Galactic latitude (deg)	R.A. (hh:mm:ss.ss)	Declination (hh:mm:ss.ss)	Distance (kpc)	Evolutionary stage	Mass ($M_\odot$)
AGAL300.218-00.111	300.218	−0.111	12:27:36.37	-62:51:24.80	4.28	Protostellar	5.3e+02
AGAL301.136-00.226	301.136	−0.226	12:35:34.81	-63:02:32.10	4.40	Protostellar	2.6e+03
AGAL302.486-00.031	302.486	−0.031	12:47:31.30	-62:53:58.00	–	HII region	4.1e+02
AGAL305.094+00.251	305.094	+0.251	13:10:12.69	-62:32:31.50	4.89	Quiescent	4.5e+02
AGAL305.209+00.206	305.209	+0.206	13:11:14.16	-62:34:42.10	4.90	Protostellar	5.2e+03
AGAL305.226+00.274	305.226	+0.274	13:11:20.07	-62:30:32.20	4.90	Protostellar	7.1e+03
AGAL305.794-00.096	305.794	−0.096	13:16:32.79	-62:49:40.60	4.97	Quiescent	1.0e+03
AGAL305.822-00.114	305.822	−0.114	13:16:48.55	-62:50:36.30	4.97	Protostellar	1.5e+03
AGAL309.236-00.457	309.236	−0.457	13:46:44.89	-62:39:00.60	3.64	Protostellar	5.5e+02
AGAL313.576+00.324	313.576	+0.324	14:20:08.30	-60:42:05.00	–	HII region	8.3e+02
AGAL313.766-00.862	313.766	−0.862	14:25:01.08	-61:44:59.40	4.09	Protostellar	1.5e+03
AGAL316.752-00.012	316.752	−0.012	14:44:51.75	-59:48:18.11	–	PDR	2.1e+04
AGAL316.764-00.012	316.764	−0.012	14:44:57.11	-59:48:01.20	2.87	Protostellar	6.2e+03
AGAL317.429-00.561	317.429	−0.561	14:51:37.80	-60:00:20.00	–	HII region	3.4e+03
AGAL318.049+00.086	318.049	+0.085	14:53:42.81	-59:08:56.50	3.62	Protostellar	1.4e+03
AGAL320.169+00.824	320.169	+0.824	15:05:17.78	-57:29:51.50	2.83	Protostellar	1.7e+03
AGAL320.232-00.284	320.232	−0.284	15:09:52.39	-58:25:37.30	4.77	Protostellar	1.9e+03
AGAL320.286-00.309	320.286	−0.309	15:10:19.26	-58:25:17.70	4.70	Protostellar	1.2e+03
AGAL322.158+00.636	322.158	+0.636	15:18:34.36	-56:38:27.50	3.88	Protostellar	5.1e+03
AGAL323.741-00.264	323.741	−0.264	15:31:46.00	-56:30:53.30	3.37	Protostellar	1.6e+03
AGAL324.718+00.341	324.718	+0.341	15:34:58.13	-55:27:23.90	3.56	Protostellar	9.5e+02
AGAL327.116-00.294	327.115	−0.294	15:50:57.18	-54:30:33.59	3.92	Quiescent	5.5e+02
AGAL328.809+00.632	328.809	+0.632	15:55:48.84	-52:43:06.20	3.03	Protostellar	1.9e+03
AGAL328.254-00.532	328.254	−0.532	15:57:59.85	-53:58:01.00	3.19	Protostellar	5.2e+03
AGAL329.184-00.314	329.184	−0.314	16:01:47.30	-53:11:41.90	3.46	Protostellar	1.6e+03
AGAL330.879-00.367	330.879	−0.367	16:10:20.30	-52:06:07.10	4.13	Protostellar	3.4e+03
AGAL331.372-00.116	331.371	−0.117	16:11:34.10	-51:35:00.13	5.42	Quiescent	1.6e+03
AGAL332.826-00.549	332.826	−0.549	16:20:10.91	-50:53:15.50	3.82	Protostellar	5.5e+03
AGAL332.962-00.679	332.962	−0.679	16:21:22.60	-50:53:01.00	3.45	Protostellar	1.6e+03
AGAL333.219-00.402	333.219	−0.402	16:21:17.67	-50:30:22.30	3.64	Protostellar	1.3e+03
AGAL333.129-00.559	333.129	−0.559	16:21:35.39	-50:40:50.10	3.98	Protostellar	1.1e+04
AGAL333.016-00.751	333.016	−0.750	16:21:56.39	-50:53:46.10	3.82	Quiescent	6.5e+02
AGAL333.481-00.224	333.481	−0.224	16:21:39.97	-50:11:43.00	3.50	Quiescent	5.7e+02
AGAL333.524-00.269	333.524	−0.269	16:22:03.39	-50:11:47.20	3.53	Quiescent	2.3e+03
AGAL335.061-00.427	335.061	−0.427	16:29:23.46	-49:12:23.90	3.01	Protostellar	1.7e+03
AGAL335.789+00.174	335.789	+0.174	16:29:47.29	-48:15:51.80	3.65	Protostellar	2.5e+03
AGAL337.342-00.119	337.342	−0.119	16:37:21.14	-47:19:26.30	4.74	Quiescent	2.5e+03
AGAL337.541-00.082	337.541	−0.082	16:37:58.48	-47:09:05.13	3.95	Quiescent	1.1e+03
AGAL337.916-00.477	337.916	−0.477	16:41:10.60	-47:08:03.00	3.23	Protostellar	1.9e+03
AGAL338.327-00.409	338.325	−0.409	16:42:27.50	-46:46:55.00	12.66	Protostellar	7.0e+03
AGAL338.869-00.479	338.869	−0.479	16:44:50.50	-46:25:01.00	3.04	Quiescent	6.7e+02
AGAL340.232-00.146	340.231	−0.147	16:48:27.56	-45:09:51.89	12.06	Quiescent	6.7e+03
AGAL340.222-00.167	340.222	−0.167	16:48:30.83	-45:11:05.79	12.04	Quiescent	7.0e+03
AGAL340.179-00.242	340.178	−0.243	16:48:40.88	-45:16:01.08	4.08	Quiescent	1.4e+03
AGAL340.398-00.396	340.397	−0.396	16:50:08.85	-45:11:49.10	3.73	Quiescent	1.6e+03
AGAL341.039-00.114	341.038	−0.114	16:51:14.11	-44:31:27.18	3.59	Quiescent	1.0e+03

Table 1. Continued

Name	Galactic longitude (deg)	Galactic latitude (deg)	R.A. (hh:mm:ss.ss)	Declination (hh:mm:ss.ss)	Distance (kpc)	Evolutionary stage	Mass ($M_\odot$)
AGAL341.702+00.051	341.702	+0.051	16:52:52.70	-43:54:24.00	–	HII region	3.9e+03
AGAL343.489-00.416	343.488	−0.416	17:01:01.19	-42:48:11.00	2.93	Quiescent	7.7e+02
AGAL345.114-00.199	345.114	−0.199	17:05:26.26	-41:22:53.50	2.90	Quiescent	3.0e+04
NGC6334-V	351.160	+0.697	17:19:57.55	-35:57:52.10	–	HII region	–
NGC6334-IV	351.240	+0.669	17:20:17.75	-35:54:55.00	–	HII region	–
NGC6334-I	351.417	+0.646	17:20:53.24	-35:46:58.00	–	Quiescent	–
AGAL010.991-00.082	10.990	−0.083	18:10:06.65	-19:27:50.66	–	Quiescent	–
AGAL014.492-00.140	14.491	−0.139	18:17:22.03	-16:25:01.93	–	Quiescent	–
AGAL018.801-00.297	18.801	−0.297	18:26:19.20	-12:41:17.00	–	Quiescent	–
AGAL022.253+00.032	22.253	+0.032	18:31:39.72	-09:28:40.60	–	Quiescent	–
G23.33-0.30	23.330	−0.300	18:34:52.30	-08:40:32.00	–	Quiescent	–
AGAL025.163-00.304	25.163	−0.304	18:38:17.20	-07:02:59.50	–	Quiescent	–
AGAL028.273-00.166	28.273	−0.166	18:43:31.00	-04:13:18.05	–	Quiescent	–
G189.1+3.0 (aka IC 443)	189.026	2.908	06:16:42.97	22:32:23.90	1.5	Unknown	–

observing sessions were completed. Observations between 21.550 and 25.057 GHz were made using the zoom-band mode of the Compact Array Broadband Backend (CABB; Wilson et al. 2011), with 64-MHz-wide bands and 32-kHz channels. Two 2-GHz-wide continuum bands were also observed. The zoom bands were chosen to cover the primary molecular emission lines of interest: the first six metastable inversion transitions of ammonia, a selection of methanol lines between 23 and 25 GHz, the 23.3-GHz thioxoethenylidene (CCS) transition, the masing water line at 22.2350798 GHz and the H67α recombination line. The resulting spectral resolution was approximately 0.4 km/s; precise parameters for each observed line are given in Table 2.

In addition to the targeted lines, other spectral lines were observed serendipitously (these included additional ammonia and methanol lines as well as other recombination lines). Details of the full set of observed (and reduced) spectral lines are shown in Table 2: in total, there were 17 molecular emission lines and six hydrogen and two helium recombination lines.

The observations were repeated using five interferometer array configurations: H75, H168, H214, 750C, and 1500C. The configuration names reflect the shortest baseline (in metres) between the array's antennas; the long-baseline data from antenna CA06 (minimum 3 000-m baseline) was included in the data reduction. The total integration times in each array configuration for the science targets are given in Table 3, along with the synthesised beam sizes (generally approximately 4.5 by 3.0 arcsec) and the RMS noise levels (averaged over all data cubes for each target, typically around 2.5 mJy/beam).

We used standard calibration sources for bandpass, flux, and phase calibration. The quasar 1253-055 was generally used for bandpass calibration, with the BL Lac object PKS 0537-441 used for early-rising sources; the bandpass calibrator was observed once per day. Flux calibration was performed using the quasar 1934-638, also observed once per day. Phase calibrators were selected from the ATCA Calibrator Database for each science target; in most cases the calibrator was shared by multiple close targets. Phase calibrators were chosen which were bright in the 15-mm band and preferably less than 5 degrees away; compromises were

resolved in favour of brightness and at the expense of distance from the target. The phase calibrators were observed every 5–15 min, depending on the prevailing atmospheric conditions and the number of targets sharing the calibrator. Overall, the weather throughout the survey was very favourable, with generally dry atmospheric conditions and low to moderate wind speeds.

4. Data reduction

The observations resulted in approximately 5 TB of raw data, which was processed using the Miriad software suite (Sault, Teuben, & Wright 1995), following the usual steps for radio-interferometry data reduction. The data were split into individual visibility files, each containing data from a single zoom band for a single source (whether calibrator or science target).

Flagging was performed on the visibility data, removing edge channels (first and last channel of each band) and spuriously high-amplitude visibilities (above 1 000 Jy for all zoom bands except that containing the masing H_2O line, for which the threshold was 100 000 Jy). RFI-affected channels were removed, followed by manual inspection of the visibility time-series to remove observations made during periods of high atmospheric instability (identified by particularly noisy or rapidly varying phase measurements), guided by the observing logs.

Bandpass and flux solutions were calculated and applied to each calibration source, and phase correction solutions then calculated. Flux calibrator observations are not available for five observing sessions (2017-07-12, 2017-07-16, 2017-09-09, 2017-09-11, 2018-08-29): on these days the flux calibration solution from the previous day (next day for 2017-07-16) was used. The calibrator solutions were then applied to the science sources.

The calibrated data from all observing sessions was then combined, and channel frequencies converted to velocities using the rest frequencies given in Table 2. Baseline continuum emission was subtracted, and a Fourier transformation performed to produce 'dirty' data cubes for each science source, for each spectral line or continuum band. A 1-arcsec pixel size was chosen, in comparison with typical beam sizes of around 3 arcsec, and 512-pixel

Table 2. Summary of molecular and recombination lines observed, and central frequency of the 2-GHz-wide broadband continuum bands. Rest frequencies, obtained from the Splatalogue (https://splatalogue.online) are from Pickett et al. 1998, with the exception of the CCS 2_1-1_0 line which is from Müller et al. 2005). Detections, at the target coordinates, are based on an SNR of 5; see Section 4 for data reduction details.

Molecular line	Rest frequency (GHz)	Resolution (kms^{-1})	Detections
NH$_3$ (1,1)	23.6944955	0.395	50
NH$_3$ (2,2)	23.7226333	0.395	29
NH$_3$ (3,3)	23.8701292	0.392	29
NH$_3$ (4,4)	24.1394163	0.388	17
NH$_3$ (5,5)	24.5329887	0.382	14
NH$_3$ (6,6)	25.0560250	0.374	12
NH$_3$ 2_1-2_1	23.0988190	0.406	12
CH$_3$OH 12_2-11_1	21.5503240	0.435	2
CH$_3$OH 9_2-10_1	23.1209150	0.405	6
CH$_3$OH 10_1-9_2	23.4447590	0.400	7
CH$_3$OH 27_2-27_1	23.8542120	0.393	2
CH$_3$OH 3_2-3_1	24.9287280	0.376	13
CH$_3$OH 4_2-4_1	24.9335040	0.376	18
CH$_3$OH 2_2-2_1	24.9344010	0.376	3
CH$_3$OH 6_2-6_1	25.0181760	0.374	5
H$_2$O 6_{16}-5_{23}	22.2350798	0.421	35
CCS 2_1-1_0	22.3440308	0.419	0

Recombination line	Rest frequency (GHz)	Resolution (kms^{-1})	Detections
H64α	24.50990328	0.382	6
H66α	22.36416629	0.419	9
H67α	21.38478489	0.438	11
H81β	23.86086423	0.393	7
H91γ	24.93980420	0.376	5
H92γ	24.14785416	0.388	4
He64α	24.51989115	0.382	2
He67α	21.39349926	0.438	4

Continuum band	Bandwidth (GHz)
Continuum 22.180 GHz	2.112
Continuum 24.060 GHz	2.112

square images were produced for each spectral channel, large enough to extract a 3-arcmin square region in Galactic coordinates. The FWHM primary beam of the ATCA at these frequencies is ∼2 arcmin. The channel images were then concatenated to form (ℓ,b,v) data cubes.

Cleaning was carried out using Miriad's two-threshold `clean` function on the central 50% of the image (linear, i.e. 50% of each spatial dimension) using 100 iterations; other settings were the `phat` parameter of 0.1, `gain` parameter of 0.1 and two `cutoff` thresholds of 5 and 1 times the dirty image RMS, as measured using `imstat` (restricted to emission-free channels). The images were then converted to Galactic coordinates, trimmed to 3-arcmin square regions, and moment 0 (integrated intensity), moment 1 (flux weighted velocity) and moment 2 (velocity dispersion) maps

derived. The spectrum at the central (target) position of each cube was also extracted for reference. Finally, the maps and data cubes were converted to FITS files.

Of the 60 sources observed, 50 were detected in the ammonia (1,1) line, 12 in all ammonia lines up to (6,6), and 18 in at least 1 methanol line. Line detection counts, using a SNR threshold of 5, for the central target locations, are given in Table 2. Radio continuum emission was observed within the field of 44 targets.

5. Derived physical properties

5.1. Model of ammonia emission

A model containing five Gaussian hyperfine line components was fitted to the ammonia (1,1) and (2,2) transition spectra, for all pixels in each map, after spatial smoothing was performed by averaging the emission over square regions 5 pixels across. The model attempts to fit the nuclear quadrupole hyperfine structure of the NH$_3$ lines (Ho & Townes 1983); it does not take into account the additional, smaller, magnetic hyperfine splitting. Since the line widths are in general much larger than this smaller splitting, modelling only the five nuclear quadrupole hyperfine lines is adequate. The model contained seven parameters: the velocity of the main hyperfine component (V_{LSR}), the full-width half-maximum amplitude line width (FWHM; common to all components) and five amplitude parameters, one for each hyperfine component, fitted independently. The satellite hyperfine component spacings are given in Table 4. Initial values of the amplitudes were 0.1 Jy/beam for the main component and 0.05 Jy/beam for the satellite components and 5 km/s for the FWHM. The initial value of the V_{LSR} was taken from the ammonia emission as follows.

The ratio of the main component amplitude to the satellite component amplitude for the ammonia (2,2) line is intrinsically larger than for the (1,1) line, due to the components' quantum statistical weights, and the (2,2) emission was readily detected for most sources. In comparison, some sources exhibited optically thick ammonia (1,1) emission, with the main component amplitude comparable to (or sometimes even lower than) the satellite component amplitudes. Thus, the velocity of the peak ammonia (2,2) emission was used as the initial estimate of V_{LSR}, where detected; otherwise, the velocity of the peak ammonia (1,1) emission was used.

Fitting was carried out by the `curve_fit` routine from the `scipy.optimize` library in Python, using the TRF ('Trust Region Reflective') algorithm. The fitted model parameters were then used to estimate the optical depth and rotational excitation temperature across each map. In addition, the model was fitted to the ammonia (3,3) emission in order to estimate the optical depth of this transition.

5.2. Optical depth

The rotational excitation temperature and optical depth were calculated from the fitted hyperfine parameters for the ammonia (1,1) and (2,2) transitions, following Mangum & Shirley (2015). Optical depth, τ, is estimated from the relative brightness of the satellite hyperfine transitions to the main component and cannot be calculated analytically. It was therefore estimated numerically from all four satellite hyperfine components simultaneously (using the

Table 3. List of integration times, in seconds, by telescope array configuration. The array configuration names (H75, for example) reflect the length of the shortest baseline in metres. The 'mean RMS' is provided as representative of the noise in the data cubes, calculated as the mean of the RMS for each target, averaged over each data cube and over all spectral lines.

Target	Total integration time (s) in array configuration:					Synthesised beam size (arcsec)	Mean RMS (mJy beam^{-1})
	H75	H168	H214	750C	1500C		
AGAL300.218-00.111	10 547	11 520	3 564	24 120	7 560	4.4×2.3	1.86
AGAL301.136-00.226	7 451	11 520	3 564	25 812	8 747	4.2×2.2	1.86
AGAL302.486-00.031	0	0	0	23 256	9 216	3.2 x 1.5	1.78
AGAL305.094+00.251	16 308	15 264	4 644	15 156	7 524	3.2×2.1	1.96
AGAL305.209+00.206	12 096	13 608	4 608	13 932	7 884	4.4×3.0	1.92
AGAL305.226+00.274	15 300	13 608	4 536	16 308	7 524	4.8×2.8	1.98
AGAL305.794-00.096	13 176	10 116	4 608	14 436	7 596	3.3×1.9	1.89
AGAL305.822-00.114	11 736	2 916	4 428	13 140	7 668	3.2×2.3	1.89
AGAL309.236-00.457	10 656	2 880	4 932	9 396	4 824	6.0×2.4	2.58
AGAL313.576+00.324	0	0	0	15 912	4 572	2.3×2.1	2.40
AGAL313.766-00.862	7 056	7 451	5 616	10 332	4 536	4.6×3.7	2.38
AGAL316.752-00.012	0	0	0	15 912	4 536	2.3×2.2	2.46
AGAL316.764-00.012	9 252	7 451	4 140	11 592	4 572	4.0×3.3	2.16
AGAL317.429-00.561	0	0	0	15 984	4 572	2.4×2.0	2.49
AGAL318.049+00.086	8 820	2 484	4 140	11 592	6 228	3.3×2.4	2.69
AGAL320.169+00.824	8 784	2 484	5 904	10 224	6 228	3.7×3.0	2.34
AGAL320.232-00.284	6 192	5 400	5 904	9 899	6 228	3.7×3.1	2.30
AGAL320.286-00.309	6 192	5 364	5 904	9 755	6 228	3.7×3.1	2.30
AGAL322.158+00.636	6 192	11 916	5 868	9 755	6 228	4.3×3.8	2.41
AGAL323.741-00.264	6 192	7 451	5 364	10 152	4 932	4.3×3.0	2.42
AGAL324.718+00.341	10 764	7 848	4 968	10 260	4 284	5.1×3.3	4.74
AGAL327.116-00.294	10 764	7 848	4 968	10 260	5 328	4.8×3.2	4.09
AGAL328.809+00.632	6 372	10 296	4 932	9 756	5 328	5.1×3.3	3.85
AGAL328.254-00.532	6 408	4 428	4 968	10 260	4 248	4.8×3.0	4.11
AGAL329.184-00.314	6 408	4 428	3 780	9 108	4 248	4.3×2.9	2.40
AGAL330.879-00.367	5 688	6 624	3 708	11 520	5 328	4.6×3.3	2.40
AGAL331.372-00.116	5 688	6 624	3 708	10 188	5 328	4.4×3.2	2.26
AGAL332.826-00.549	8 280	9 432	3 708	9 288	5 328	4.3×3.2	2.50
AGAL332.962-00.679	5 652	14 004	3 708	9 108	5 328	4.6×3.9	2.29
AGAL333.219-00.402	8 100	9 108	4 932	4 968	5 328	4.5×4.2	2.81
AGAL333.129-00.559	5 364	13 212	8 460	20 520	4 716	4.3×3.1	1.93
AGAL333.016-00.751	5 652	10 656	5 004	16 416	3 780	4.6×3.0	2.18
AGAL333.481-00.224	5 616	10 044	4 824	16 308	4 716	4.4×3.0	2.25
AGAL333.524-00.269	5 616	10 656	4 788	19 080	3 780	4.3×3.1	2.12
AGAL335.061-00.427	5 796	11 664	5 184	11 160	5 328	4.7×4.0	2.34
AGAL335.789+00.174	5 796	11 664	5 112	11 160	5 328	4.7×3.8	2.33
AGAL337.342-00.119	7 884	11 736	4 968	14 076	3 780	4.8×3.7	2.71
AGAL337.541-00.082	7 848	6 876	4 968	15 120	4 752	4.3×3.4	2.51
AGAL337.916-00.477	4 896	6 084	4 968	11 880	12 456	3.6×2.8	2.00
AGAL338.327-00.409	4 896	5 652	4 248	11 555	5 904	4.0×3.2	2.58
AGAL338.869-00.479	4 644	5 616	4 212	11 555	4 968	4.1×3.2	2.60
AGAL340.232-00.146	5 616	4 896	4 248	9 324	3 780	4.4×3.0	3.00
AGAL340.222-00.167	5 616	10 008	4 248	9 504	3 312	5.0×4.1	3.27
AGAL340.179-00.242	6 048	5 292	4 428	9 540	3 348	4.5×3.2	3.36
AGAL340.398-00.396	6 624	6 228	4 248	10 187	3 780	4.7×3.8	3.12

Table 3. Continued

Target	Total integration time (s) in array configuration:					Synthesised beam size	Mean RMS
	H75	H168	H214	750C	1500C		
	(s)	(s)	(s)	(s)	(s)	(arcsec)	(mJy beam^{-1})
AGAL341.039-00.114	6 624	10 908	4 248	6 300	3 312	5.6×4.9	3.60
AGAL341.702+00.051	0	0	0	7 956	3 312	3.4×1.9	3.16
AGAL343.489-00.416	8 460	4 968	4 032	10 008	3 312	4.3×3.0	2.87
AGAL345.114-00.199	8 280	10 008	4 032	10 008	3 312	5.0×3.9	3.08
NGC6334-V	0	0	0	11 556	0	4.4×2.5	4.35
NGC6334-IV	0	0	0	9 468	0	4.1×2.5	4.87
NGC6334-I	0	0	0	20 268	0	4.5×2.2	3.48
AGAL010.991-00.082	11 664	12 672	6 336	8 208	6 012	7.9×3.0	2.58
AGAL014.492-00.139	6 048	6 192	6 084	8 208	5 904	9.2×2.5	2.74
AGAL018.801-00.297	2 664	4 715	6 048	8 568	5 724	11.6×2.3	3.34
AGAL022.253+00.032	4 500	10 944	6 732	10 692	5 472	11.4×3.3	3.72
G23.33-0.30	1 656	4 715	6 696	10 619	5 040	14.9×2.1	3.77
AGAL025.163-00.304	4 500	10 944	6 660	10 619	4 896	17.0×2.0	3.12
AGAL028.273-00.166	4 500	10 908	8 387	11 124	4 896	27.6×1.7	4.24
G189.1+3.0 (aka IC 443)	0	0	0	15 947	0	5.324×1.661	3.68

Table 4. Velocity of ammonia hyperfine components, relative to the main component, used in the 5-component hyperfine model.

Transition	Left outer (kms^{-1})	Left inner (kms^{-1})	Main (kms^{-1})	Right inner (kms^{-1})	Right outer (kms^{-1})
NH$_3$ (1,1)	−19.36	−7.74	0	7.74	19.36
NH$_3$ (2,2)	−25.78	−16.57	0	16.57	25.78

Levenberg–Marquardt algorithm to minimise the sum-of-squares error between the data and the model); an initial value of $\tau = 1.0$ was used.

Let $T_R(m)$ and $T_R(s)$ be the measured intensity of the main and satellite hyperfine components, respectively, and $\tau_{(1,1)}$ the optical depth of the main component of the ammonia (1,1) emission. We obtained $\tau_{(1,1)}$ by solving

$$\frac{T_R(m)}{T_R(s)} = \frac{1 - \exp(-\tau_{(1,1)})}{1 - \exp(-A\tau_{(1,1)})} \tag{1}$$

simultaneously for the inner ($A = \frac{5}{18}$) and outer ($A = \frac{2}{9}$) hyperfine components; the sum-of-squares error for the four components was minimised to obtain the best fit. The published data set (see Section 8) also contains estimated optical depths for ammonia (2,2) ($A_{\text{inner}} = 0.0651$, $A_{\text{outer}} = 0.0628$) and (3,3) ($A_{\text{inner}} = 0.03$, $A_{\text{outer}} = 0.0296$).

5.3. Rotational excitation temperature

Using $\tau_{(1,1)}$ and the FWHM for the (1,1) and (2,2) transitions, $\Delta v_{(1,1)}$ and $\Delta v_{(2,2)}$, respectively, the excitation temperature was then calculated (Mangum & Shirley 2015) using the brightness temperature of the NH$_3$ (1,1) and (2,2) transitions, $T_{B,(1,1)}$ and $T_{B,(2,2)}$, respectively, as

$$T_{ex}((2,2);(1,1))$$
$$= \frac{-41.5}{\ln\left[-\frac{0.283\Delta v_{(2,2)}}{\tau_{(1,1)}\Delta v_{(1,1)}}\ln\left(1 - \frac{T_{B,(2,2)}}{T_{B,(1,1)}}(1 - \exp[-\tau_{(1,1)}])\right)\right]}. \tag{2}$$

The statistical errors for the ammonia (1,1), (2,2), and (3,3) optical depths and for the rotational excitation temperature were computed using a bootstrapping Monte Carlo approach. For each model parameter, a random value was drawn 1 000 times from a Gaussian distribution with mean equal to the optimal parameter value and variance equal to the variance of the parameter estimates, as reported by the fitting routine. The optical depth and excitation temperature were then calculated using each set of random parameters, and the mean and variance of the resulting distributions calculated to estimate the uncertainty of these derived values. These values are included in the data release; variances for the optical depth are typically below 0.1 and below 2 for the excitation temperature.

The rotational excitation temperatures calculated from the CACHMC data at the target locations have a mean of 19.42 and range of 11.37–28.38. These values in agreement with previously reported data: for example, Urquhart et al. (2011) reports a mean of 19.3 and range of 10.2–39.0 for a large sample of similar massive star-forming regions. Line widths are also in accord to those previously reported, with a mean of 3.03 (range 0.57–10.43) in the CACHMC data, compared with 1.9 (range 0.2–7.8) (Urquhart et al. 2011.)

Table 5. Positions of masers identified in the CACHMC survey. Each maser can be found in the data cube referred to in the column 'Map name'. Galactic longitude and latitude are given in degrees, velocities in km/s and maximum intensity in mJy. These sources were identified as masers on the basis of their narrow line width, brightness, and point-source-like nature. (c) candidate maser: identification as a maser is not certain. Rest frequencies for the lines are given in Table 2.

n	Map name	Galactic longitude (deg)	Galactic latitude (deg)	Peak velocity (kms^{-1})	Maximum intensity (mJy beam^{-1})	Maser line	(note)
1	AGAL010.991-00.082	11.006	−0.069	27.965	160.82	NH$_3$ (3,3)	
2	AGAL014.492-00.139	14.49	−0.137	41.072	65.812	NH$_3$ (3,3)	
3	AGAL014.492-00.139	14.49	−0.138	41.464	61.365	NH$_3$ (3,3)	
4	AGAL305.209+00.206	305.192	0.205	−40.646	85.87	NH$_3$ (3,3)	
5	AGAL305.209+00.206	305.20884	0.20415	−39.86	172.42	NH$_3$ (3,3)	(c)
6	AGAL316.764-00.012	316.764	−0.012	−38.69	357.9	NH$_3$ (3,3)	
7	AGAL323.741-00.264	323.74	−0.261	−52.432	63.699	NH$_3$ (3,3)	
8	AGAL323.741-00.264	323.741	−0.261	−52.432	51.059	NH$_3$ (3,3)	(c)
9	AGAL324.718+00.341	324.716	0.339	−53.196	102.68	NH$_3$ (3,3)	
10	AGAL324.718+00.341	324.71	0.344	−51.628	54.021	NH$_3$ (3,3)	
11	AGAL328.254-00.532	328.237	−0.546	−40.284	59.358	NH$_3$ (3,3)	(c)
12	AGAL329.184-00.314	329.181	−0.303	−49.411	60.87	NH$_3$ (3,3)	
13	AGAL333.524-00.269	333.523	−0.275	−49.942	117.23	NH$_3$ (3,3)	
14	AGAL337.916-00.477	337.912	−0.475	−43.581	252.78	NH$_3$ (3,3)	
15	AGAL337.916-00.477	337.92	−0.475	−40.837	85.5	NH$_3$ (3,3)	(c)
16	AGAL338.327-00.409	338.327	−0.411	−37.549	97.036	NH$_3$ (3,3)	
17	AGAL340.232-00.146	340.241	−0.158	−51.705	33.675	NH$_3$ (3,3)	
18	AGAL340.398-00.396	340.374	−0.39	−42.769	71.89	NH$_3$ (3,3)	
19	G23.33-0.30	23.325	−0.304	56.247	3673.3	NH$_3$ (3,3)	
20	NGC6334-I	351.423	0.644	−6.862	3049.9	NH$_3$ (3,3)	
21	NGC6334-IV	351.243	0.671	−3.6	164.08	NH$_3$ (3,3)	
22	NGC6334-IV	351.238	0.664	−3.6	59.652	NH$_3$ (3,3)	
23	NGC6334-IV	351.248	0.67	−3.6	73.241	NH$_3$ (3,3)	
24	NGC6334-V	351.159	0.706	−7.558	1010	NH$_3$ (3,3)	
1	NGC6334-I	351.417	0.646	8.926	102.97	NH$_3$ (6,6)	
1	NGC6334-V	351.16048	0.69755	−7.66	46.71	CH$_3$OH 2-2	(c)
2	G23.33-0.30	23.325205	−0.30344	67.69	85.25	CH$_3$OH 2-2	
1	AGAL305.209+00.206	305.20273	0.20721	−41.99	53.14	CH$_3$OH 3-3	
2	AGAL320.286-00.309	320.28575	−0.30854	−65.42	57.83	CH$_3$OH 3-3	
3	AGAL333.129-00.559	333.14107	−0.57199	1.08	23.85	CH$_3$OH 3-3	(c)
4	AGAL333.129-00.559	333.12634	−0.57309	−53.44	23.06	CH$_3$OH 3-3	(c)
5	AGAL333.219-00.402	333.22018	−0.40262	−51.35	66.93	CH$_3$OH 3-3	
6	NGC6334-IV	351.24426	0.6695	−2.36	132.34	CH$_3$OH 3-3	
7	NGC6334-IV	351.25037	0.65145	1.4	58.33	CH$_3$OH 3-3	(c)
8	NGC6334-IV	351.24981	0.65145	−0.48	61.46	CH$_3$OH 3-3	(c)
1	AGAL300.218-00.111	300.21769	−0.10886	−38.85	37.19	CH$_3$OH 4-4	
2	AGAL305.209+00.206	305.20273	0.20721	−41.81	839.61	CH$_3$OH 4-4	
3	AGAL313.576+00.324	313.57622	0.32441	−47.25	310.95	CH$_3$OH 4-4	
4	AGAL313.766-00.862	313.75302	−0.86436	−52.05	50.87	CH$_3$OH 4-4	
5	AGAL320.169+00.824	320.16717	0.82075	−39.43	72.54	CH$_3$OH 4-4	
6	AGAL320.286-00.309	320.28575	−0.30854	−65.24	160.17	CH$_3$OH 4-4	
7	AGAL328.254-00.532	328.25663	−0.5316	−43.83	38.64	CH$_3$OH 4-4	(c)
8	AGAL328.254-00.532	328.25607	−0.53076	−43.83	33.14	CH$_3$OH 4-4	(c)
9	AGAL332.962-00.679	332.96326	−0.67804	−46.84	45.83	CH$_3$OH 4-4	

Table 5. Continued

n	Map name	Galactic longitude (deg)	Galactic latitude (deg)	Peak velocity (kms^{-1})	Maximum intensity (mJy beam^{-1})	Maser line	(note)
10	AGAL333.219-00.402	333.22018	−0.40262	−51.17	390.44	CH$_3$OH 4-4	
11	NGC6334-V	351.15798	0.69922	−5.6	57.77	CH$_3$OH 4-4	
12	NGC6334-IV	351.24426	0.6695	−2.18	1578.27	CH$_3$OH 4-4	
13	NGC6334-IV	351.25037	0.65145	1.58	293.27	CH$_3$OH 4-4	
14	NGC6334-IV	351.24981	0.65145	−0.3	603.67	CH$_3$OH 4-4	
15	AGAL014.492-00.139	14.48955	−0.13681	41.42	65.66	CH$_3$OH 4-4	
16	AGAL025.163-00.304	25.16023	−0.29983	73.38	37.89	CH$_3$OH 4-4	
1	AGAL333.219-00.402	333.22046	−0.402901	−51.01	372.29	CH$_3$OH 6-6	
1	NGC6334-I	351.41676	0.64535	−11.91	6960	CH$_3$OH 9-10	
2	NGC6334-V	351.16048	0.69699	−5.88	59.14	CH$_3$OH 9-10	(c)
1	AGAL305.209+00.206	305.20273	0.20721	−42.57	1269.87	CH$_3$OH 10-9	
2	AGAL330.879-00.367	330.87777	−0.36687	−58.42	37.08	CH$_3$OH 10-9	(c)
3	AGAL330.879-00.367	330.87694	−0.3677	−58.02	39.41	CH$_3$OH 10-9	(c)
4	AGAL330.879-00.367	330.86999	−0.38216	−63.22	53.79	CH$_3$OH 10-9	(c)
1	AGAL010.991-00.082	11.005918	−0.068548	24.12	1462.16	H$_2$O 6_{16}-5_{23}	
2	AGAL014.492-00.139	14.478428	−0.14626	8.71	69.81	H$_2$O 6_{16}-5_{23}	
3	AGAL025.163-00.304	25.164123	−0.30372	65.24	113.32	H$_2$O 6_{16}-5_{23}	
4	AGAL028.273-00.166	28.280005	−0.1536	66.53	250.11	H$_2$O 6_{16}-5_{23}	
5	AGAL300.218-00.111	300.21686	−0.11053	−64.27	318.64	H$_2$O 6_{16}-5_{23}	
6	AGAL301.136-00.226	301.13611	−0.22526	−42.26	41.29	H$_2$O 6_{16}-5_{23}	
7	AGAL302.486-00.031	302.48675	−0.03192	−31.19	6183.87	H$_2$O 6_{16}-5_{23}	
8	AGAL305.209+00.206	305.20828	0.2061	−46.48	32620	H$_2$O 6_{16}-5_{23}	
9	AGAL305.226+00.274	305.22272	0.27471	−38.03	13812.24	H$_2$O 6_{16}-5_{23}	
10	AGAL305.794-00.096	305.79531	−0.09636	−35.73	116.77	H$_2$O 6_{16}-5_{23}	
11	AGAL305.822-00.114	305.82252	−0.11469	−36.47	602.12	H$_2$O 6_{16}-5_{23}	
12	AGAL305.822-00.114	305.81724	−0.11136	−43.62	404.52	H$_2$O 6_{16}-5_{23}	
13	AGAL305.822-00.114	305.81668	−0.10969	−50.78	220.07	H$_2$O 6_{16}-5_{23}	
14	AGAL309.236-00.457	309.25215	−0.47292	−18.16	49.72	H$_2$O 6_{16}-5_{23}	
15	AGAL313.576+00.324	313.57705	0.32497	−39.5	42030.98	H$_2$O 6_{16}-5_{23}	
16	AGAL313.766-00.862	313.76692	−0.86241	−55.09	514338	H$_2$O 6_{16}-5_{23}	
17	AGAL316.764-00.012	316.76275	−0.011643	−34.82	29111	H$_2$O 6_{16}-5_{23}	
18	AGAL317.429-00.561	317.42911	−0.55596	31.44	1717.47	H$_2$O 6_{16}-5_{23}	
19	AGAL317.429-00.561	317.42883	−0.56069	22.6	357.38	H$_2$O 6_{16}-5_{23}	
20	AGAL318.049+00.086	318.04975	0.086671	−51.37	172535	H$_2$O 6_{16}-5_{23}	
21	AGAL320.169+00.824	320.16717	0.82102	−32.56	1284.92	H$_2$O 6_{16}-5_{23}	
22	AGAL320.232-00.284	320.23133	−0.28384	−65.1	18849	H$_2$O 6_{16}-5_{23}	
23	AGAL320.286-00.309	320.2852	−0.308816	−67.21	5490	H$_2$O 6_{16}-5_{23}	
24	AGAL322.158+00.636	322.15803	0.63611	−73.01	54224	H$_2$O 6_{16}-5_{23}	
25	AGAL322.158+00.636	322.16498	0.62443	−52.38	5030	H$_2$O 6_{16}-5_{23}	
26	AGAL323.741-00.264	323.74007	−0.26267	−50.87	10057	H$_2$O 6_{16}-5_{23}	
27	AGAL324.718+00.341	324.71641	0.34195	−44.81	13237	H$_2$O 6_{16}-5_{23}	
28	AGAL327.116-00.294	327.11295	−0.29123	−61.1	91.99	H$_2$O 6_{16}-5_{23}	
29	AGAL328.254-00.532	328.25552	−0.53132	−42.1	16010	H$_2$O 6_{16}-5_{23}	
30	AGAL328.254-00.532	328.25413	−0.53243	−50.1	12410	H$_2$O 6_{16}-5_{23}	

Table 5. Continued

n	Map name	Galactic longitude (deg)	Galactic latitude (deg)	Peak velocity (kms^{-1})	Maximum intensity (mJy beam^{-1})	Maser line	(note)
31	AGAL328.254-00.532	328.23523	−0.54827	−42.1	93 783	$H_2O\ 6_{16}$-5_{23}	
32	AGAL329.184-00.314	329.18299	−0.31382	−50.65	79 483	$H_2O\ 6_{16}$-5_{23}	
33	AGAL330.879-00.367	330.87833	−0.36687	−61.58	110 880	$H_2O\ 6_{16}$-5_{23}	
34	AGAL332.826-00.549	332.82585	−0.54924	−60.17	126 795	$H_2O\ 6_{16}$-5_{23}	
35	AGAL332.962-00.679	332.96326	−0.67915	−56.97	3 221	$H_2O\ 6_{16}$-5_{23}	
36	AGAL332.962-00.679	332.96132	−0.67609	−54.44	885.81	$H_2O\ 6_{16}$-5_{23}	
37	AGAL332.962-00.679	332.94186	−0.68582	−52.76	2 698	$H_2O\ 6_{16}$-5_{23}	
38	AGAL333.129-00.559	333.13134	−0.56004	24.46	2 357.6	$H_2O\ 6_{16}$-5_{23}	
39	AGAL333.129-00.559	333.13023	−0.5592	−52.58	5 223.8	$H_2O\ 6_{16}$-5_{23}	
40	AGAL333.219-00.402	333.22074	−0.40207	−54.69	519.38	$H_2O\ 6_{16}$-5_{23}	
41	AGAL333.524-00.269	333.52591	−0.26629	−53.28	892.75	$H_2O\ 6_{16}$-5_{23}	
42	AGAL335.061-00.427	335.05938	−0.42742	−43.35	15 451	$H_2O\ 6_{16}$-5_{23}	
43	AGAL335.061-00.427	335.0655	−0.42825	−38.72	860.09	$H_2O\ 6_{16}$-5_{23}	
44	AGAL335.789+00.174	335.78698	0.17697	−54.77	17 640	$H_2O\ 6_{16}$-5_{23}	
45	AGAL335.789+00.174	335.78892	0.17391	−68.66	3 900.4	$H_2O\ 6_{16}$-5_{23}	
46	AGAL337.342-00.119	337.35952	−0.11318	−17.48	174.88	$H_2O\ 6_{16}$-5_{23}	
47	AGAL337.342-00.119	337.35618	−0.13708	−41.06	124.27	$H_2O\ 6_{16}$-5_{23}	
48	AGAL337.916-00.477	337.91539	−0.47671	−33.71	192 165	$H_2O\ 6_{16}$-5_{23}	
49	AGAL338.327-00.409	338.32492	−0.408919	−42.91	7 101	$H_2O\ 6_{16}$-5_{23}	
50	AGAL340.232-00.146	340.24112	−0.15792	−53.42	605.9	$H_2O\ 6_{16}$-5_{23}	
51	AGAL340.398-00.396	340.37355	−0.39019	−44.56	359.37	$H_2O\ 6_{16}$-5_{23}	
52	AGAL340.398-00.396	340.37355	−0.38853	−47.08	190.05	$H_2O\ 6_{16}$-5_{23}	
53	AGAL340.398-00.396	340.37327	−0.3863	−36.14	168.63	$H_2O\ 6_{16}$-5_{23}	
54	AGAL343.489-00.416	343.4888	−0.41558	−26.79	41.56	$H_2O\ 6_{16}$-5_{23}	
55	NGC6334-I	351.41815	0.64618	−7.5	12 145 449	$H_2O\ 6_{16}$-5_{23}	
56	NGC6334-IV	351.24315	0.67117	−89.34	1 154 078	$H_2O\ 6_{16}$-5_{23}	
57	NGC6334-V	351.1602	0.697	−7.71	56 302	$H_2O\ 6_{16}$-5_{23}	

5.4. Hyperfine anomalies

The fitted hyperfine component amplitudes were used to examine the so-called 'hyperfine anomaly' (HFA) for ammonia (1,1), wherein the left and right outer satellite hyperfine components are not equally strong, and similarly for the inner components: theory predicts that each pair should be of equal integrated intensity under LTE excitation. This effect was observed on the maps of at least 36 sources: as previous observations had shown (see, for example, Stutzki et al. 1984; Garay & Lizano 1999; Longmore et al. 2007; Camarata, Jackson, & Chambers 2015), HFAs were found to be common at the peak of ammonia emissions. In this survey, however, observations of the extended, fainter, ammonia emission revealed that the HFA is also present in those regions and appears to be spatially varying.

Maps of the HFA (inner and outer ratios) are included in the data release. These were calculated using integrated intensity (spatially smoothed by averaging emission over square regions 5 pixels across) from the targets' ammonia (1,1) data cubes. Each component was summed over velocities within 10 channels of the hyperfine component velocity, with spacings as given in Table 4

and based on the fitted radial velocity, and within 8 channels for the main (central) component (not used for the ratio calculations but provided in the data release).

6. Masers

Many of the observed spectral bands included molecular line transitions capable of masing. These include ammonia (3,3), ammonia (6,6), water 6_{16}-5_{23} and multiple methanol transition lines. The lines, locations, velocities, and peak flux of detected masers and maser candidates are given in Table 5. These sources were identified as masers on the basis of their narrow line width, brightness and point-source-like nature. Examples of maser spectra observed are shown in Fig. 1.

Multiple ammonia masers were observed, including two previously unknown ammonia (3,3) masers in the 'Nessie Nebula' (Jackson et al. 2010), near the positions of the dense clumps AGAL337.916-00.477 ('Nessie A', Fig. 1(a)) and AGAL338.327-00.409 ('Nessie C'). A previously known ammonia (6,6) maser in NGC6334-I was confirmed (Beuther et al. 2007, Fig. 1(b)).
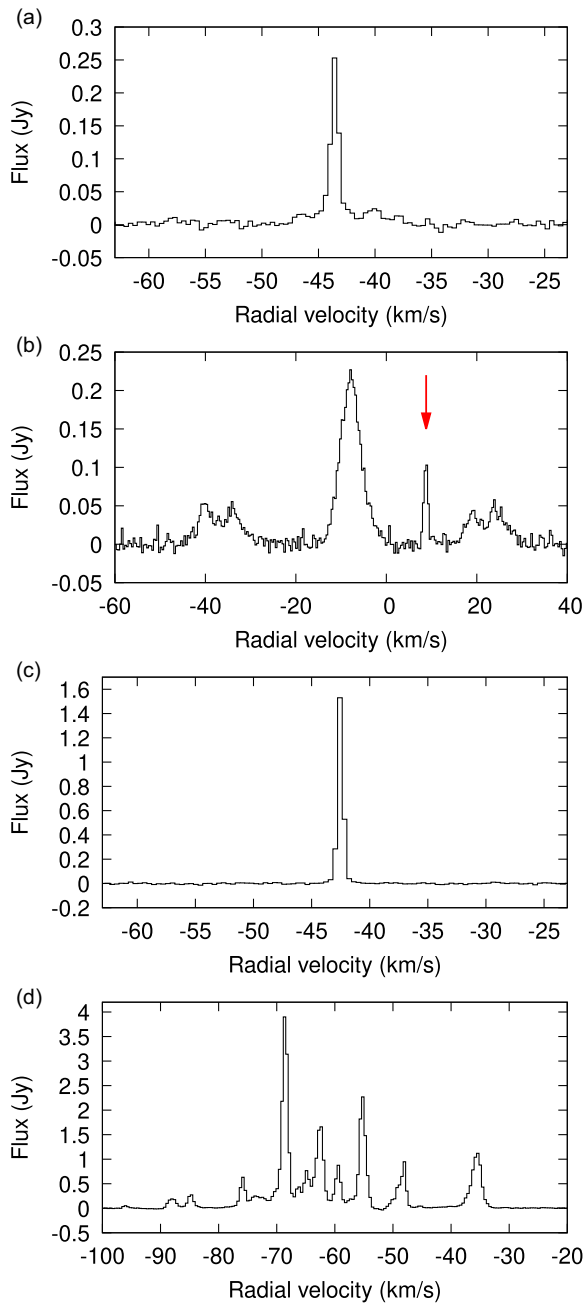
Figure 1. Spectra of selected masers detected during the survey. (a) AGAL337.916-00.477 ('Nessie A') NH_3 (3,3) maser; (b) NGC6334-I NH_3 (6,6) maser, at 8.926 km/s (indicated by the red arrow: other emission is thermal); (c) AGAL305.209+00.206 CH_3OH 10-9 maser; (d) AGAL335.789+00.174 H_2O 6_{16}-5_{23} maser. Channel widths are approximately 0.4 ms^{-1}. The masers can be found in these targets' data cubes; coordinates of the maser sites are given in Table 5.

Figure 2. A map of the 22.180-GHz continuum emission for AGAL337.916-00.477 ('Nessie A'); contours show the moment 0 ammonia (1,1) emission (contour values are 1, 50, 200, and 500 mJy/beam).

Masers were observed in 6 methanol transition lines. The survey detected Type I methanol masers in the 2-2, 3-3, 4-4, 6-6, and 10-9 transitions and Type II methanol masers in the 9_2-10_1 transition.

The methanol 10-9 transition is a very rare masing line, first detected in 2011 (Voronkov et al. 2011). We observed a maser at this frequency near AGAL305.209+00.206 (Fig. 1(c)), and three candidate maser sites near AGAL330.879-00.367. Type II methanol masers, in the rare CH_3OH 9_2-10_1 masing line at 23.121

GHz, were detected near NGC6334-I and NGC6334-V; the former has been observed previously (Cragg et al. 2004).

The H_2O 22.2350798-GHz spectral line is a common maser transition that indicates shocks associated with star-forming regions. Water masers were detected towards 43 of the 60 observed clumps, often slightly displaced from the ammonia emission peaks. Almost all of these exhibited multiple velocity components: one of the sites near AGAL335.789+00.174 contains at least 12 distinct peaks at different velocities (Fig. 1(d)).

The data release contains the spectra of the detected masers and candidates and maps showing the position of the masers relative to the ammonia (1,1) emission for each target.

7. Data examples

7.1. Example source: AGAL337.916-00.477

This section presents data for one science target, AGAL337.916-00.477, a dense clump associated with the infrared-dark filament known as the 'Nessie Nebula' (Jackson et al. 2010). This target is of great interest as a potential massive star-forming site. Ammonia emission in the Nessie Nebula has been previously studied (see, for example, Goodman et al. 2014; Purcell et al. 2012; Zucker, Battersby, & Goodman 2015). We hereafter refer to this source as 'Nessie A'.

Nessie A is a hot protostellar source, containing a previously unknown ammonia (3,3) maser (see Fig. 1(a)). A map of its ammonia (1,1) and 22.180-GHz continuum emission is shown in Fig. 2. It is turbulent, with very high spectral line widths, hot, as all observed ammonia transition lines are strong, and has high optical depth. Maps of the measured line width for NH_3 (1,1), estimated rotational excitation temperature (using NH_3 (1,1) and (2,2)) and the optical depth of the NH_3 (1,1) main component emission are shown in Fig. 3. The line spectra at the target coordinates of Nessie A are shown in Fig. 4.

Nessie A contains many features of interest in the CACHMC data. These include extended ammonia emission from the (1,1) transition up to the (6,6) transition, a 22- and 24-GHz continuum point source and extended continuum emission. Ammonia (3,3) and water masers are present and line widths vary from very high in the central region (7–8 kms^{-1} FWHM) to narrow (1–2 kms^{-1} FWHM) in the extended emission. In addition, Nessie A
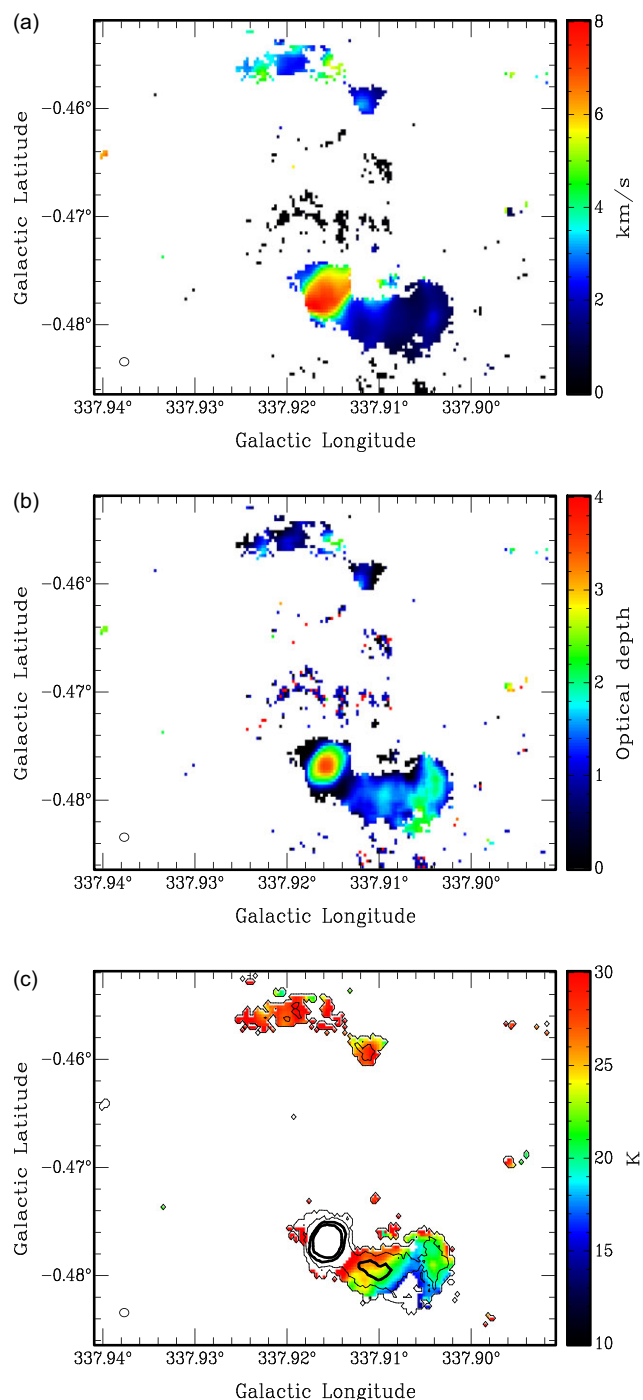
Figure 3. Maps showing derived physical properties of AGAL337.916-00.477 ('Nessie A'): (a) full-width half-maximum line width, (b) optical depth, and (c) excitation temperature, T_{ex} (with NH$_3$ (1,1) contours as in Fig. 2 included for reference). At the peak of ammonia emission, near (337.915°, -0.478°), the derived temperature becomes non-physical, since the NH$_3$ (2,2) emission is stronger than (1,1): the assumption of LTE is broken, assuming a single gas component. The beam, 3.6 × 2.8 arcsec across, is shown as a small ellipse in the lower left-hand corner of each map.

exhibits the ammonia HFA described in Section 5.4, for both inner and outer hyperfine components; the ratio of inner components is shown in Fig. 5.
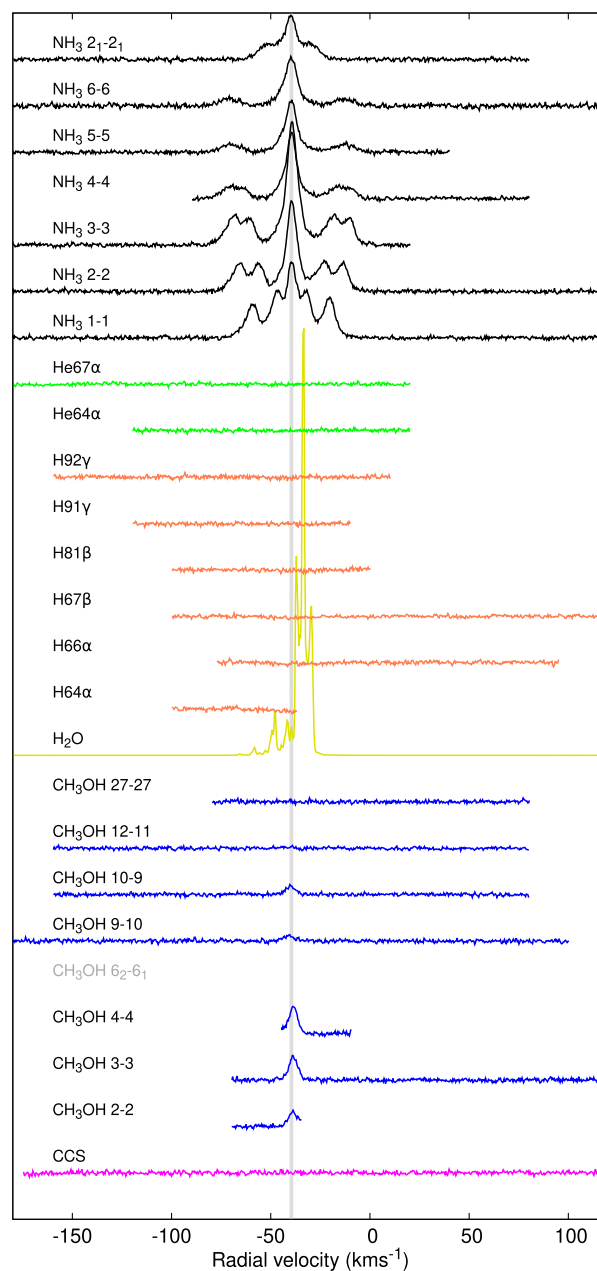
Figure 4. A combined plot of transition lines at the target position of AGAL337.916-00.477 ('Nessie A'). Lines are all shown at the same scale (except for the masing H$_2$O line, shown in yellow, whose emission has been down-scaled by 100X) and have been vertically offset from each other by 0.2 Jy/beam. The data is aligned to radial velocity: a vertical bar has been added at the target's systemic velocity (−39.58 km/s) to aid visual interpretation. The plotted velocity range of the data reflects the number of channels in each transition line's data cube, which varies. Note that there is no CH$_3$OH 6_2-6_1 data for this target: it lies outside the velocity limits of the receiver band for this line. Line colours distinguish the different molecules and atoms.

7.2. Absorption lines

The survey revealed interesting absorption features against the free-free continuum emission from a central H II region. Such absorption was most prominent at the central positions of AGAL301.136-00.226, AGAL328.809+00.632, and AGAL332.826-00.549, with strong absorption in all ammonia lines. Absorption features were prominent at off-centre positions
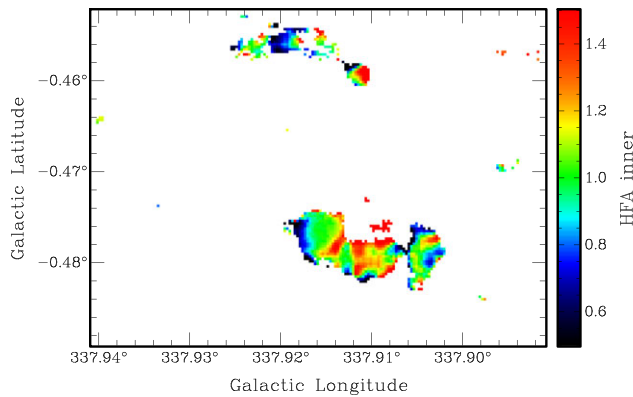
Figure 5. A map of the NH_3 (1,1) hyperfine anomaly, showing the ratio of the left inner hyperfine component to the right inner hyperfine component, for AGAL337.916-00.477 ('Nessie A'). The relative velocities of the components are given in Table 4.

for AGAL320.232-00.284, AGAL322.158+00.636 and NGC6334-IV, but only for the NH_3 (1,1) and (2,2) lines. The central spectra for AGAL301.136-00.226 are shown in Fig. 6, where absorption in all ammonia and most methanol lines can be seen. In addition, an unexpected absorption feature in the 22.23 GHz water line was observed for AGAL328.809+00.632, at the same radial velocity as the ammonia absorption features. This feature is shown in Fig. 7.

8. Data release

The CACHMC data[b] (https://doi.org/10.25919/74nw-9r95) is available to download from the CSIRO's Data Access Portal, at https://data.csiro.au/collection/csiro:59354. The project website at https://cachmc.space provides galleries of moment maps and central spectra.

The files included in the data release are arranged into five directories, each (except `masers/`) containing a subdirectory for each science target:

- `data/`: data cubes and derived moment maps, RMS maps and central spectra;
- `hfa/`: ammonia (1,1) hyperfine anomaly maps; and
- `ircontext/`: mid-infrared context images overlaid with ammonia (1,1) emission contours;
- `masers/`: catalogue and spectra of detected masers.
- `temperature/`: derived temperature and optical depth maps;

In addition to the observations detailed in Section 3, continuum data was collected at 5.5 GHz and 9.0 GHz for 15 targets exhibiting strong 22- and 24 GHz continuum emission; these observations were undertaken during weather unsuitable for the usual, higher frequency, observations. The raw data for these observations (as well as all other CACHMC raw data) are available in CSIRO's Australia Telescope Online Archive[c] (ATOA) with the project code 'C3152'.

Details of the directory structure and the included files in the data release are given in Appendix 9.
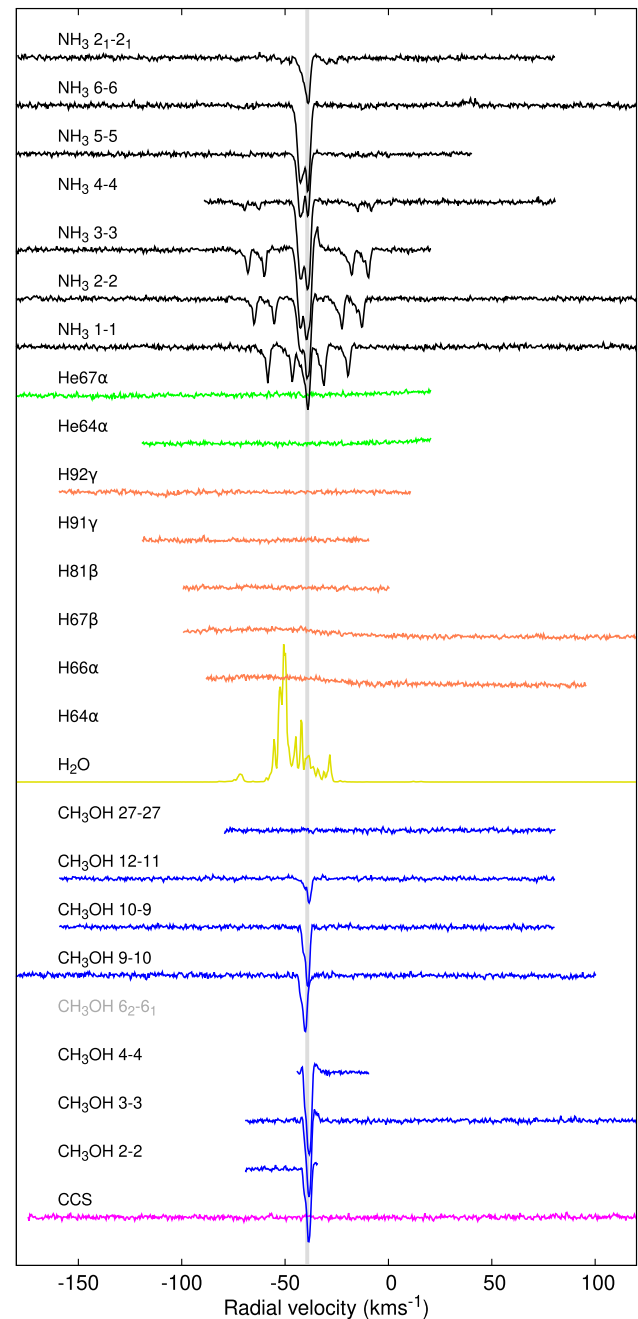
Figure 6. A combined plot of transition lines for AGAL301.136-00.226. Strong absorption can be seen in the ammonia and methanol spectral bands, along with evidence of emission at the edge of the CH_3OH 3-3 and 4-4 absorption features. The target exhibits ammonia emission close to the absorption velocity. Lines are all shown at the same scale (except for the masing H_2O line, whose emission has been down-scaled by 100X) and have been vertically offset from each other by 0.2 Jy/beam. The data is aligned to radial velocity: a vertical bar has been added at the target's systemic velocity (-39.2850 kms^{-1}) to aid visual interpretation. The plotted velocity range of the data reflects the number of channels in each transition line's data cube, which varies. Note that there is no CH_3OH 6_2-6_1 data for this target: they lie outside the velocity limits of the receiver band for this line. Line colours distinguish the different molecules and atoms.

9. Summary

The CACHMC Legacy Survey was carried out on the ATCA over four winter observing seasons and successfully observed 60
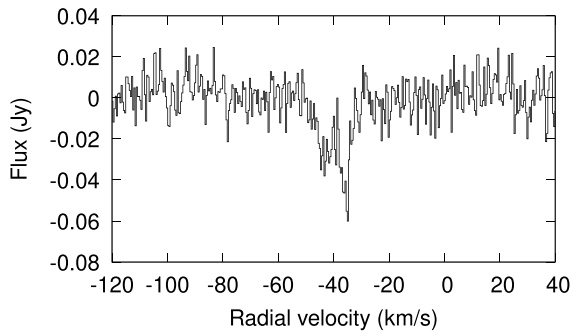
Figure 7. Absorption feature in the 22-GHz water spectral band for AGAL328.809+00.632; it is almost central to the map, lying 1–2 arcsec away from the position of maximum ammonia absorption, and the radial velocity of this absorption feature matches the radial velocity of emission and absorption in other spectral lines.

potential sites of future high-mass star formation. High signal-to-noise ratio data for ammonia (J,K) = (1,1) through (6,6) transitions were collected, and 24 ammonia (3,3) masers identified, along with 19 spectral lines (including H_2O and methanol masing lines). Continuum emission was measured at 22 and 24 GHz. Ammonia HFAs were observed and found to be common, as previous studies have shown, but also occurring in spatially extended molecular gas.

Data products from the survey have been prepared and include FITS data cubes for the observed spectral lines, along with central spectra and moment 0, 1, and 2 maps for the 60 targets. These observations are now available to characterise the turbulent structure within the target clumps and to measure the locations, temperatures, masses, temporal sequence and kinematics of their individual star-forming cores.

Competing interests. None.

Data availability statement. The CACHMC data (https://doi.org/10.25919/74nw-9r95) is available to download from the CSIRO's Data Access Portal at https://data.csiro.au/collection/csiro:59354.

References

Aguirre, J. E., et al. 2011, ApJS, 192, 4
Benjamin, R., Churchwell, E., & Babler, B. 2003, PASP, 115, 953
Billington, S. J., Urquhart, J. S., Figura, C., Eden, D. J., & Moore, T. J. T. 2019, MNRAS, 483, 3146
Camarata, M. A., Jackson, J. M., & Chambers, E. 2015, ApJ, 806, 74
Carey, S. J., et al. 2009, PASP, 121, 76
Churchwell, E., et al. 2009, PASP, 121, 213
Contreras, Y., et al. 2013, A&A, 549, A45
Cragg, D. M., et al. 2004, MNRAS, 351, 1327
Dunham, M. K., Rosolowsky, E., Evans, N. J., Cyganowski, C., & Urquhart, J. S. 2011, ApJ, 741, 110
Garay, G., & Lizano, S. 1999, PASP, 111, 1049
Glenn, J., et al. 2009, in ASP Conference Series, Vol. 417, Submillimeter Astrophysics and Technology: A Symposium Honoring Thomas G. Phillipsed, ed. D. C. Lis, J. E. Vaillancourt, P. F. Goldsmith, T. A. Bell, N. Z. Scoville, & J. Zmuidzinas (San Francisco: Publications of the Astronomical Society of the Pacific), 277

Goodman, A. A., et al. 2014, ApJ, 797, 53
Guzmán, A. E., et al., 2015, ApJ, 815, 130
Ho, P. T. P., & Townes, C. H. 1983, ARA&A, 21, 239
Hoare, M. G., et al. 2012, PASP, 124, 939
Jackson, J. M., Finn, S. C., Chambers, E. T., Rathborne, J. M., & Simon, R. 2010, ApJL, 719, L185
Jackson, J. M., et al. 2013, PASA, 30, 57
Jackson, J. M., et al. 2024, ApJ, 965, 187
Joye, W. A., & Mandel, E. 2003, in ASP Conference Series, Vol. 295, Astronomical Data Analysis Software and Systems XII, ed. H. E. Payne, R. I. Jedrzejewski, & R. N. Hook (San Francisco, CA: ASP), 489
Kraemer, K. E., & Jackson, J. M., 1995, ApJ, 439, 9
Li, S., et al. 2022, ApJ, 939, 102
Longmore, S. N., Burton, M. G., Barnes, P. J., Wong, T., Purcell, C. R., & Ott, J. 2007, MNRAS, 379, 535
Mangum, J. G., & Shirley, Y. L. 2015, PASA, 127, 266
McEwen, B. C., Pihlström, Y. M., & Sjouwerman, L. O. 2016, ApJ, 826, 189
Molinari, S., et al. 2010, PASP, 122, 314
Motte, F., Bontemps, S., & Louvet, F. 2018, AnnRevA&A, 56
Motte, F., et al. 2022, A&A, 662, A8
Müller, H.S.P., Schlöder, F., Stutzki, J., & Winnewisser, G. 2005, JMS, 742, 215
O'Neill, T. J., Cosentino, G., Tan, J. C., Cheng, Y., & Liu, M. 2021, ApJ, 916, 45
Pickett, H. M., et al. 1998, JQSRT, 60, 883
Purcell, C. R., et al. 2012, MNRAS, 426, 1972
Rathborne, J. M., et al. 2016, PASA, 33, 30
Sabatini, G., et al. 2022, ApJ, 936, 80
Sanhueza, P., et al. 2019, ApJ, 886, 102
Sault, R. J., Teuben, P. J., & Wright, M. C. H. 1995, in Astronomical Society of the Pacific Conference Series, Vol. 77, Astronomical Data Analysis Software and Systems IV, R. A.Shaw, H. E. Payne, & J. J. E. Hayes, 433
Schuller, F., et al. 2009, A&A, 504, 415
Stutzki, J., Jackson, J. M., Olberg, M., Barrett, A. H., & Winnewisser, G. 1984, A&A, 139, 258
Urquhart, J. S., et al. 2011, MNRAS, 418, 1689
Urquhart, J. S., et al. 2014, MNRAS, 443, 1555
Vázquez-Semadeni, E., Palau, A., Ballesteros-Paredes, J., Gómez, G. C., & Zamora-Avilés, M. 2019, MNRAS, 490, 3061
Voronkov, M. A., et al. 2011, MNRAS, 413, 2339
Walsh, A. J., et al. 2011, MNRAS, 416, 1764
Whitaker, J. S., et al. 2018, AJ, 154, 140
Wienen, M., Wyrowski, F., Schuller, F., Menten, K. M., Walmsley, C. M., Bronfman, L., & Motte, F. 2012, A&A, 544, A146
Wienen, M., et al. 2018, A&A, 609, A125
Wilson, W. E., et al. 2011, MNRAS, 416, 832
Zucker, C., Battersby, C., & Goodman, A. 2015, ApJ, 815, 23

Appendix: Structure of published data

A. Directory: `data/`

The reduced observational data is contained in the `data/` directory. There is a subdirectory for each science target, containing a subdirectory for each spectral band. Within the spectral band subdirectories are files with the following extensions, for each of the spectral lines (listed in Table 2):

- `.cube.fits`: data cube FITS file
- `.mom0.fits`: moment 0 FITS file
- `.mom0.png`: moment 0 map
- `.autoscaled.mom0.png`: moment 0 map
- `.mom1.fits`: moment 1 FITS file

- `.mom1.png`: moment 1 map
- `.autoscaled.mom1.png`: moment 1 map
- `.mom2.fits`: moment 2 FITS file
- `.mom2.png`: moment 2 map
- `.autoscaled.mom2.png`: moment 2 map
- `.rms.fits`: RMS map FITS file
- `.rms.png`: RMS map image
- `.centralspectrum.png`: plot of the line spectrum at the target coordinates
- `.centralspectrum.txt`: text file containing the spectrum at the target coordinates

Directories for the two continuum bands contain only the integrated intensity FITS file and map images. From the spectral line data cubes, the RMS of each cleaned cube was calculated, using channels identified as signal-free across all sources. For some targets not all channels were available (due to their systemic velocity). Moment map images have been masked at a signal-to-noise ratio of 5.

The FITS files and PNG images with spatial dimensions are 3 arcmin square, in Galactic coordinates centred on the target's location. The autoscaled images use a colour range derived from the minimum and maximum values; non-autoscaled images use a colour range from -0.1 to 1 Jy to aid comparison between targets (-0.005 to 0.05 Jy for the continuum files).

B. Directory: `hfa/`

The `hfa/` directory contains ammonia (1,1) HFA map images, along with the integrated intensity files used to produce them. The integrated intensity at each point was spatially smoothed by averaging over a square $5{\times}5$-pixel region. The maps show the left outer to right outer and the left inner to right inner NH_3 (1,1) hyperfine integrated intensity ratios, with a subdirectory for each target; the displayed range in each map is 0.2–2.0. Files with the following extensions are provided:

- `.HFAinner.fits`: inner hyperfine intensity ratio (left inner:right inner)
- `.HFAinner.png`: inner hyperfine intensity ratio map
- `.HFAouter.fits`: outer hyperfine intensity ratio (left outer:right outer)
- `.HFAouter.png`: outer hyperfine intensity ratio map
- `.leftInnerII.fits`: integrated intensity of the left inner NH_3 (1,1) hyperfine component
- `.leftOuterII.fits`: integrated intensity of the left outer NH_3 (1,1) hyperfine component
- `.mainII.fits`: integrated intensity of the main NH_3 (1,1) hyperfine component
- `.rightInnerII.fits`: integrated intensity of the right inner NH_3 (1,1) hyperfine component
- `.rightOuterII.fits`: integrated intensity of the right outer NH_3 (1,1) hyperfine component

The hyperfine intensity ratio maps have been masked at a signal-to-noise ratio of 5.

C. Directory: `ircontext/`

Mid-infrared context images from the Spitzer Space Telescope are included for each target, using data from the GLIMPSE (Benjamin et al. 2003; Churchwell 2009) and MIPSGAL (Carey et al. 2009) surveys of the Galactic Plane. The red, green and blue channels show MIPS 24-μm, IRAC 8-μm and IRAC 3.6-μm emission, respectively, and contours show the ammonia (1,1) emission, drawn between the minimum and maximum integrated intensity values.

The context images were created using DS9 (Joye & Mandel 2003), with 12 contour linearly spaced contour levels drawn, using the 'minmax' scale, so that the lowest contour is at the minimum value of the data and the highest contour is at the maximum value of the data, with 10 evenly spaced contours in between. The contours were drawn with a spatial smoothing parameter of 3. Due to the dynamic range of the ammonia (1,1) emission, these contours do not represent the data as easily as the moment 0 maps, but the context and location of the targets in their local Galactic environment is shown.

D. Directory: `masers/`

The `masers/` directory contains a tab-separated catalogue file listing detected masers along with the spectrum at each detected location. The spectrum is provided both as a plot of brightness versus velocity (in the `maserspectra/` subdirectory) and as a text file containing the same data (in the `maserspectratxt/` subdirectory).

The `masermaps/` subdirectory contains a contour map of the ammonia (1,1) integrated intensity for each science target with detected masers, overlaid with markers (listed in the file `legend.txt`) distinguishing the various masing molecules.

File names begin with the target name (referring to the data cube in which the maser can be found), followed by a letter (a, b, c, . . .), if required, to distinguish multiple masers of the same line on the same map, and an abbreviation of the spectral line of the maser.

E. Directory: `temperature/`

Best-fit model parameters for ammonia (1,1), (2,2), and (3,3) emission spectra, along with the derived optical depths and rotational excitation temperature (using ammonia (1,1) and (2,2)), are contained in the `temperature/` directory. These derived values were calculated from the data cubes, spatially smoothed by averaging over a square $5{\times}5$-pixel region. There is a subdirectory for each science target, containing files with the following extensions for ammonia (1,1), (2,2), and (3,3):

- `.SSE.fits`: model fitting sum-of-squares error
- `.fwhm.fits`: fitted FWHM
- `.fwhm_variance.fits`: fitting variance of FWHM
- `.tau.fits`: estimated optical depth from best-fit model parameters
- `.tau.png`: estimated optical depth map image
- `.tauMean.fits`: mean value of optical depth from bootstrapped error estimates
- `.tauVar.fits`: variance of optical depth from bootstrapped error estimates

- `.v0.fits`: fitted radial velocity
- `.v0_variance.fits`: fitting variance for radial velocity

In addition to these model and derived values, the rotational excitation temperature, calculated using ammonia (1,1) and (2,2) emission, is given in files with the following extensions:

- `.nh3.Tex.fits`: estimated rotational excitation temperature

- `.nh3.Tex.png`: estimated rotational excitation temperature map
- `.nh3.TexMean.fits`: mean rotational excitation temperature from bootstrapped error estimates
- `.nh3.TexVar.fits`: variance of rotational excitation temperature from bootstrapped error estimates

The optical depth and rotational excitation temperature maps have been masked at a signal-to-noise ratio of 5.